

Coherent emission from single impurities in ZnSe through resonant excitation

Yuxi Jiang,^{1,2} Christine Falter,^{3,4} Robert M. Pettit,¹ Nils von den Driesch,^{3,4} Yurii Kutovyi,^{3,4} Amirehsan Alizadeh Herfati,^{1,2} Alexander Pawlis,^{3,4} and Edo Waks^{1,2}

¹Institute for Research in Electronics and Applied Physics and Joint Quantum Institute, University of Maryland, College Park, Maryland 20742, USA

²Department of Electrical and Computer Engineering, University of Maryland, College Park, Maryland 20740, USA

³Peter-Grünberg-Institute (PGI-9), Forschungszentrum Jülich GmbH, 52425 Jülich, Germany

⁴JARA-FIT (Fundamentals of Future Information Technology), Jülich-Aachen Research Alliance, 52062 Aachen, Germany

Abstract

Impurity-bound excitons in II-VI semiconductors are promising optically active solid-state spin qubit systems. Previous work relied on incoherent optical excitation to generate photons from these impurities. However, many quantum applications require resonant driving to directly excite optical transitions and maintain coherence. Here, we demonstrate coherent optical emission from a resonantly driven single impurity-bound exciton in ZnSe. We observe resonance fluorescence and verify the emission coherence through polarization interferometry. Resonant excitation also enables the direct measurement of the Debye-Waller factor, determined to be 0.94, indicating high efficiency emission to the zero-phonon line. Time-resolved resonance fluorescence measurements reveal a fast optically driven ionization process attributed to Auger recombination, along with a slower spontaneous ionization process having a lifetime of 21 μ s due to charge tunneling from the impurity. We demonstrate that a low-power incoherent pump laser efficiently stabilizes the charge of the impurity-bound exciton on the timescale of 9.3 ns. Our results pave the way for direct coherent optical and spin control through resonant excitation of impurity-bound excitons in II-VI semiconductors.

Introduction

Impurity-bound excitons in II-VI semiconductors are promising candidates for optically active qubits due to their bright emission and potentially long coherence times¹⁻⁷. Among these materials, shallow donor-bound excitons in ZnSe stand out for their ability to generate bright and indistinguishable single-photon emission^{5,7,8}. Zn and Se also possess a high natural abundance of spin-0 isotopes that can be even isotopically purified to create an almost entirely, nuclear spin-free environment, ideal for spin qubits⁹. Moreover, ZnSe can be grown in epitaxial thin films that can be patterned into nanophotonic devices which enhance light-matter interaction and single photon efficiency^{7,10,11}.

Virtually all optical studies of impurity-bound excitons in ZnSe have relied on incoherent excitation of the emitters using above-band pumping^{5-7,10,11}. This approach suffers from random time-jitter associated with carrier relaxation and also induces fluctuating electric fields, both of which create optical decoherence and broaden the emission linewidth. Furthermore, incoherent excitation cannot probe the internal energy level structure of the emitter. Resonant excitation mitigates these problems by directly driving transitions between the quantum states of the emitter¹²⁻¹⁵. In this approach, a narrow bandwidth tunable laser selectively pumps an isolated quantum state on-resonance to produce elastically scattered fluorescence emission. However, to date, such coherent emission from individual impurity states has yet to be reported.

In this letter, we demonstrate resonance fluorescence and coherent emission from a single impurity-induced donor-bound exciton. The impurity is a Cl atom embedded in a ZnSe quantum well, engineered into a nanopillar structure that exhibits bright single photon emission⁵. Polarization interferometry reveals quantum interference between the single photon emission of the impurity and the resonant laser, demonstrating coherence between these light sources. Through resonant excitation we measure the Debye-Waller factor to be 0.94, one of the highest values reported for defect emitters. Time-resolved measurements of resonantly pumped donor-bound exciton reveal both a rapid optically induced ionization process, which we attribute to the Auger recombination, and a slower spontaneous discharging of the impurity state. We show that a low-power above-band laser stabilizes the charge of the impurity state and recovers the charge on a

rapid timescale of 9.3 ns. Our results provide a new optical toolbox for generating coherent emission and directly manipulating the electronic states of impurity-bound excitons.

Main text

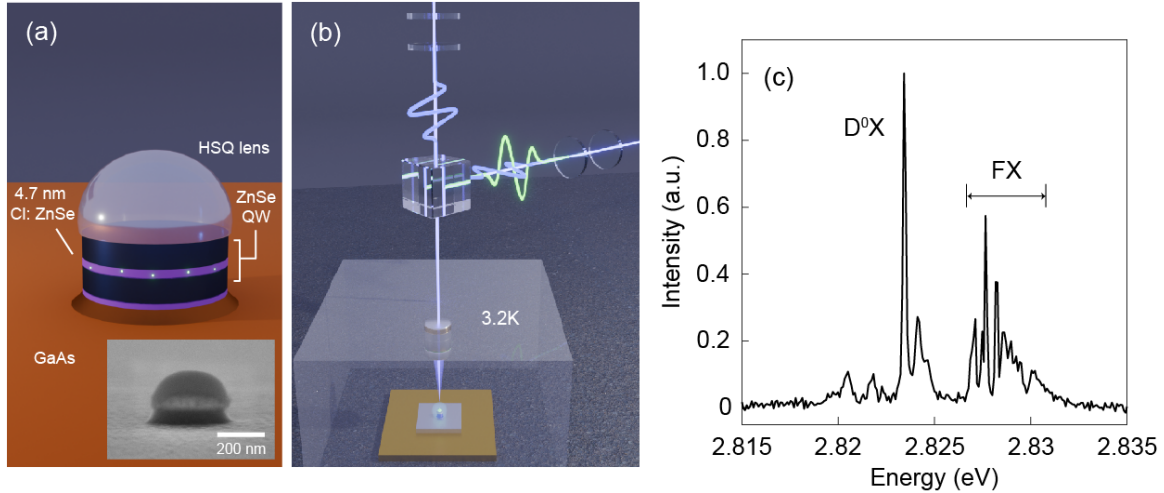


Figure 1. Optical excitation of a Cl impurity bound exciton in a ZnSe nanopillar. (a) A schematic of the nanopillar device. Inset shows scanning electron microscope image of fabricated device. (b) resonant excitation and fluorescence detection scheme. (c) Photoluminescence spectrum from the ZnSe nanopillar under an above-band excitation at 3.06 eV (405 nm). The spectrum shows free exciton (FX) and donor-bound exciton (D^0X) emission lines.

The schematic in Figure 1a illustrates the device, which consists of a ZnSe nanopillar fabricated on Cl delta-doped ZnMgSe/ZnSe/ZnMgSe quantum well (QW) structures. We fabricate an HSQ nanolens on top of the nanopillar to enhance the out-coupling efficiency of the emission⁷. The Methods section provides a detailed description of the device. The inset shows a scanning electron microscope image of the fabricated device.

Figure 1b shows a schematic of the experimental measurement technique. We cool the sample to 3.2 K using a closed-cycle refrigerator. We excite the sample using a confocal microscope configuration. For resonant excitation, we use a cross-polarized detection scheme to reject stray reflection from the sample surface. The Methods section contains a detailed description of the measurement technique.

We initially characterize the device through photoluminescence measurements. We pump the sample using a 3.06 eV (405 nm) laser diode, whose energy is higher than the ZnSe and ZnMgSe bandgaps. Figure 1c shows the resulting spectrum. We observe a group of peaks ranging from 2.827 eV to 2.832 eV that correspond to the free exciton emission. A narrow peak at 2.8233 eV labeled as D^0X corresponds to a single donor-bound exciton emission⁷. Supplementary Material Section I provides additional photoluminescence measurements that characterize the emitter polarization states and determine the above-band saturation power to be 2.9 μW .

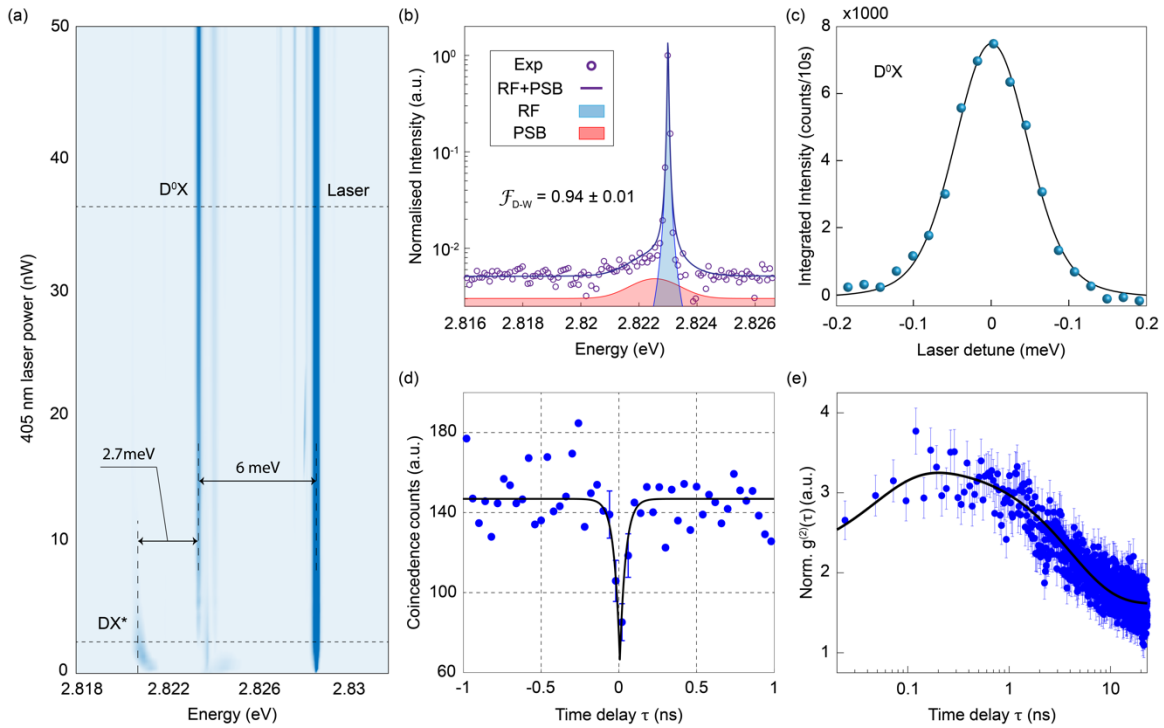


Figure 2. Resonance fluorescence from an impurity-bound exciton in ZnSe. (a) Photoluminescence-excitation spectrum of the Cl-doped ZnSe nanopillar. The tunable laser pumps free exciton at 2.829 eV with a power of 30 nW, while the above-band laser (3.06 eV) power is varying from 0 to 50 nW. Fluorescence emits from the donor-bound exciton state as the above-band pump power exceeds 4 nW. Another state labeled as DX^* appears when the power is less than 4 nW. (b) Fluorescence spectrum of the resonantly pumped impurity-bound exciton. The spectrum normalizes to the maximum intensity of the emission peak. (c) Energy-detuned resonant excitation of the bound exciton and the resonance fluorescence spectrum. The solid markers show experimental fluorescence data. The solid line shows a Voigt function fit to the experimental data. The above-band laser has a constant power of 32 nW. (d) Coincidence counts histogram of the resonance fluorescence as a function of time delay. The resonant pumping power is 100 nW. The binning size is 40 ps. (e) Correlation function towards long-time delay up to 20 ns.

Although we see clear emission when performing above-band excitation, we observe very little emission from the impurity bound exciton line when driving the free-exciton emission line. These results are consistent with previous work,⁵ which showed that driving the impurity-bound exciton through the free-exciton line requires an additional small amount of above-band power. Figure 2a shows the measured photoluminescence spectrum as a function of the above-band laser power, with the external cavity laser tuned to the free-exciton line and set to a fixed power of 30 nW. The bright line at 2.829 eV corresponds to direct reflection of the excitation laser light. When the above-band laser power is below 3 nW, we do not observe any emission from the donor-bound exciton line. Instead, we observe a weak emission peak at 2.818 eV labeled as DX*. This peak exhibits a noticeable red-shift as with increasing above-band power. We observe fluorescence from the donor-bound exciton state (2.823 eV) when the above-band power exceeds 4 nW, coupled with a drop in the DX* intensity. From these measurements we ascertain that without above-band excitation, the donor-bound exciton discharges, forming a positive-charged donor-bound exciton, or other ionized donor complexes¹⁶. Introduction of the above-band laser generates free-carriers which effectively raises the fermi-level, thereby stabilizing the charge of the neutral donor-bound exciton.

From the measurements, we determine that 32 nW of above-band laser is sufficient to stabilize the charge. The above-band laser is well below the saturation power of the donor-bound exciton and generates negligible photoluminescence (~2.2% of total fluorescence count). Supplementary Materials Section II provides additional measurements where we tune the tunable laser over the free-exciton emission spectrum. The bound-exciton emission shows strong emission when the laser is resonant with the free-exciton line, and quickly decays away from resonance. These measurements further demonstrate that the emission results from the creation of free excitons.

Next we show resonant driving of the emitter by tuning the laser at 10 nW excitation power directly to the donor-bound exciton line. We reject background from direct reflection of the pump laser using cross-polarization (see Methods), which has an extinction ratio exceeding 10^6 . To prevent the impurity from discharging, we add 32 nW of above-band laser. This above-band power is sufficient to stabilize the charge but produces negligible fluorescence, as demonstrated in Figure 2a.

Figure 2b shows the measured spectrum with resonant excitation, plotted on a semilogarithmic scale. The open circles represent the measured spectrum, which exhibits a bright emission peak at the laser energy (at 2.823 eV, same as the donor-bound exciton line) corresponding to the resonance fluorescence from the emitter. We also observe a broader peak detuned from the center of the resonance fluorescence line, which is attributed to a phonon sideband. The phonon sideband may arise from the acoustic phonons in ZnSe, whose coupling strength to the emitter can be enhanced by QW confinement¹⁷⁻¹⁹, while the LO-phonons coupling is suppressed²⁰. We fit the measured spectrum to a sum of a Lorentzian function for the resonance fluorescence, and Gaussian function which represents a good model for the phonon sideband²¹. The blue curve and red curve show the fitted results from the Lorentzian and Gaussian respectively, while the black solid line shows the total fit which exhibits excellent agreement with the measured data. From the fit, we can extract the Debye-Waller factor of the emitter, which is the ratio of elastically scattered fluorescence intensity to total emission intensity of the emitter. We calculate this factor as $\mathcal{F}_{DW} = I_{RF}/(I_{RF} + I_{PSB})$, where I_{RF} and I_{PSB} are the areas under the fit for the resonance fluorescence and phonon sideband respectively. Using the data from the fit in Figure 2b, we obtain $\mathcal{F}_{DW} = 0.94$, which is among the highest in reported defect quantum emitters²²⁻²⁴. Supplementary Section III provides temperature-dependent measurements of the resonantly pumped bound exciton, which show an increased phonon sideband at higher temperature.

To validate that the bright sharp emission in Figure 2b corresponds to resonance fluorescence, we measure the resonant emission as a function of resonant laser detuning. Figure 2c shows the measured results for a 10 nW resonant laser power. Blue circles represent integrated intensity of the reflected resonant laser measured with a 32 nW above-band laser, while the solid line is a numerical fit to a Voigt function. We see a clear resonant behavior where emission is maximum at the donor-bound exciton energy, and quickly falls off with detuning. In contrast, we perform the same scan with no above-band laser where the impurity is discharged, and the result only shows background light due to imperfect cross-polarization (See Supplementary Material Section III). From the fit of the resonance fluorescence peak we obtain a linewidth of $0.12 \text{ meV} \pm 7.8 \text{ } \mu\text{eV}$. This linewidth is 35 times broader than the lifetime limited linewidth of $3.43 \text{ } \mu\text{eV}$ (given by $\Gamma_0 =$

$1/(2\pi\tau_{\text{rad}})^{5,25}$, $\tau_{\text{rad}} = 192 \text{ ps}^5$). We attribute the broadened linewidth to spectral wandering²⁶, which may arise from charge fluctuations of defects and trap states near the Cl impurity²⁷.

To demonstrate the quantum nature of the resonance fluorescence emission, we perform second-order intensity correlation measurements on the resonance fluorescence. We excite the donor-bound exciton state on-resonance with a laser power of 100 nW. The signal is detected using an intensity correlation setup with two superconducting nanowire single photon detectors (see Methods for details). Both detectors have an average counts rate of 5×10^3 counts/sec, with a background signal of 1.1×10^3 counts/sec. The noise signal originates from both the finite cross-polarization filtering of the resonant laser and the above-band excited photoluminescence and is evaluated by pumping the emitter with two laser sources individually.

Figure 2d shows the measured coincidence counts within a short timescale. At zero time-delay it exhibits clear anti-bunching, demonstrating the quantum nature of the emission. We fit the measurements to an exponential curve as $A(1 - (1 - q_0)e^{-|\tau|/\tau_0})$, where τ_0 is a parameter determined by the radiative decay rate and the pumping power²⁸. The parameter q_0 represents the zero-time delay correlation value. From the fit, we obtain $q_0 = 0.37 \pm 0.11$. The single photon purity is limited by the background noise. We define the signal to background noise as $R = S/(S + B)$, where S is the signal count rate and B is the background count rate. Based on the detector count rate value, we attain $R = 0.85$. By subtracting to the background, we obtain a background-corrected q_0 of 0.13 (see Supplementary Material Section IV for details).

Figure 2e shows second-order correlation function over a longer time window on a semilogarithmic scale. The correlation exhibits significant bunching. This bunching effect suggests that the impurity bound exciton blinks^{29,30}. We model the blinking by treating the emitter as switching between two states, one which emits and one that is dark, with switching rates of k_{on} and k_{off} ^{29,31}. When the blinking rate is much lower than the radiative decay rate of the bound exciton, the long-time bunching can be separately modeled as an exponential function of the form $g_{\text{long}}^{(2)}(\tau) = 1 + \left(\frac{k_{\text{off}}}{k_{\text{on}}}\right) e^{-|\tau|/\tau_1}$, where $\tau_1 = 1/k_{\text{on}} + 1/k_{\text{off}}$ ^{29,30,32}. We use a combined correlation function $g_{\text{total}}^{(2)}(\tau) = g_{\text{short}}^{(2)}(\tau) \times g_{\text{long}}^{(2)}(\tau)$, where $g_{\text{short}}^{(2)}(\tau) = 1 - (1 - q_0)e^{-|\tau|/\tau_0}$, to fit the

experimental data (See Supplementary Material Section IV for details) as shown by Figure 2e. From the fit we determine a correlation time of the bunching to be 4.05 ns with the on to off ratio as 0.27.

To investigate the coherence of the resonance fluorescence emission, we implement a single-beam polarization interferometry. Under resonant excitation, the resonance fluorescence field is given by $E_{\text{RF}} = \frac{\gamma}{-i\Delta + \frac{\gamma}{2}} \sqrt{\mu} E_0$, where γ is the atomic transition decay rate, Δ is the laser detune, E_0 is the electric field amplitude of the excitation laser, and μ is the fluorescence efficiency. The equation shows that both the amplitude and phase of the resonance fluorescence varies as a function of laser detuning. The phase of the resonance fluorescence at a detuning of $\Delta \ll -\gamma$ experiences a π phase shift relative to that of $\Delta \gg \gamma$. As the excitation energy is swept across the resonance of the zero-phonon line of the bound exciton, there is a rapid phase change between these two conditions. This phase change can be probed by a polarization interferometry^{33,34}. In our experiment, we mix the resonance fluorescence of the emitter to a local oscillator generated by pulling a fraction of light from the excitation laser. We accomplish this mixing by rotating the input quarter waveplate in the cross-polarization setup, which modulates both the intensity and relative phase of the local oscillator (see Methods).

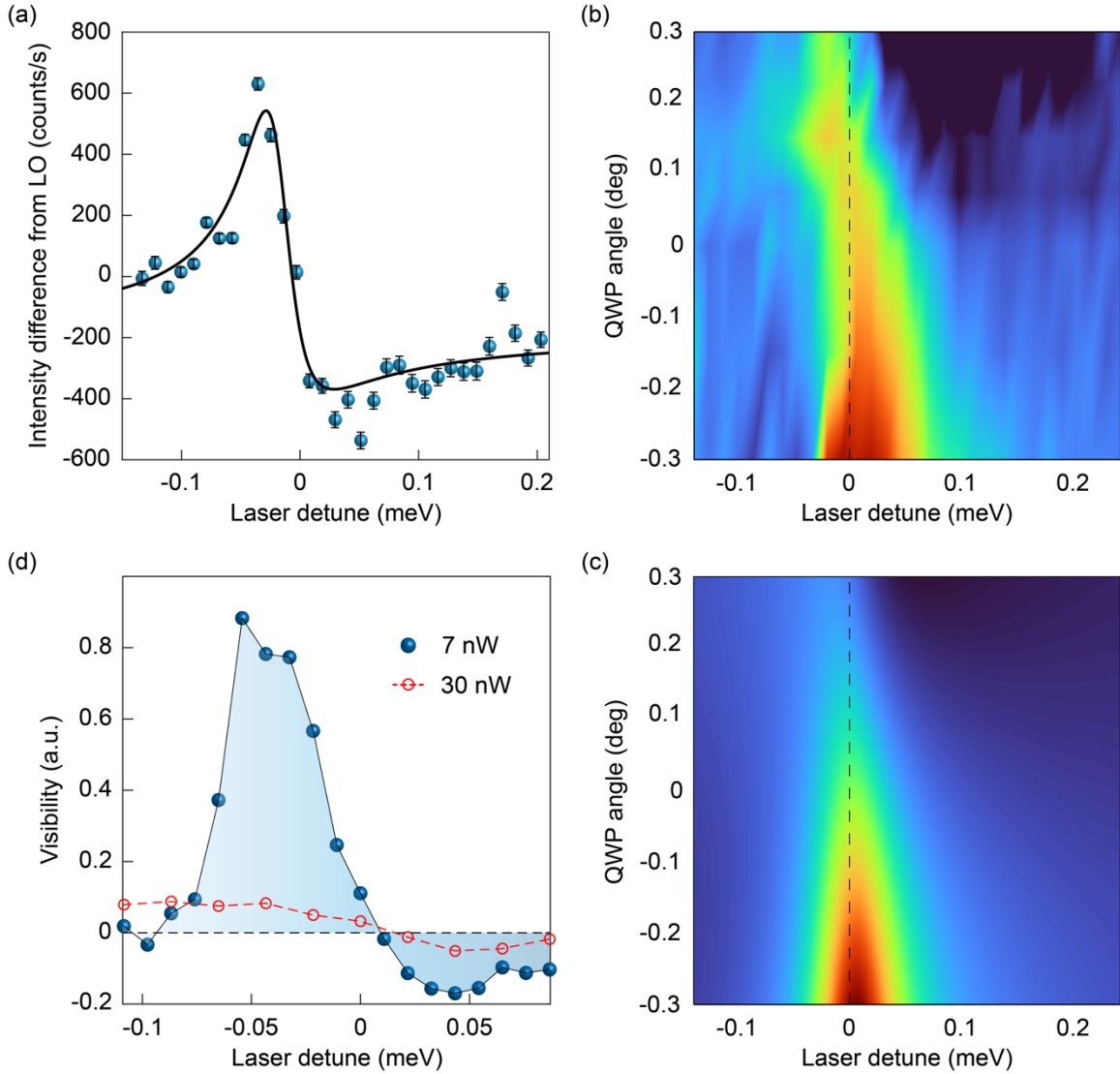


Figure 3. Polarization interferometry demonstrating the coherence of the resonance fluorescence. (a) Measurement of the interference effect by mixing the resonance fluorescence with a local oscillator, obtained by rotating the quarter-wave plate with an angle of +0.3-degree from the optimized cross-polarization condition. The result is subtracted to the local oscillator intensity. The lines show a numerical fit to the theoretical model. (b) Reflection spectra at different quarter-wave plate angles. (c) A numerical calculation from the model shows a good match to the measurement results. The dashed lines denote the zero laser detune energy. (d) At +0.5-degree, two resonant scanning spectra at different laser powers of 7 nW (blue solid circles) and 30 nW (red open circles) are shown. For both measurements, above-band excitation power of 12 nW is applied to the sample.

Figure 3a shows results of the polarization interferometry measurement at quarter-wave plate angle of 0.3-degree. We measure the resonant laser reflection intensity I_{tot} with using both resonant laser and the above-band excitation, and then subtract it to the local oscillator intensity I_{LO} obtained with only using the resonant laser. The circles denote the measured data of intensity difference.

The resulting spectrum exhibits a Fano-resonance³⁵ pattern. At lower energies we observe a peak with the maximum energy position shifting from the original resonance fluorescence peak position (centered at 0-energy detune), indicating constructive interference. At higher energies, we observe destructive interference, where the total intensity I_{tot} from the mixing of the fluorescence with the local oscillator is less than the local oscillator intensity I_{LO} . This rapid transition from constructive to destructive interference validates the phase coherence of the emission. We fit both curves to a theoretical model as described in the Supplementary Material Section V, which exhibits good agreement.

Figure 3b shows the interference spectrum as a function of the input quarter-wave plate angle, while Figure 3c shows the calculated values from the theoretical model described in Supplementary Materials Section V. Both experiment and theory exhibit excellent agreement. As we rotate the quarter-wave plate, we vary the phase and strength of the local oscillator simultaneously. At an angle greater than +0.1-degree, clear evidence of interference transition from lower energies to higher energies is obtained. When rotating the waveplate to negative angles, we instead observe clear peak position shift, as well as constructive interference at blue-detuned energies. There is also weak destructive interference at the red-detuned energies. The asymmetry arising between the positive and negative quarter-wave plate orientation is because the local oscillator field amplitude and relative phase shift varies asymmetrically. We illustrate this effect by additional simulation results and discussion in the Supplementary Material Section V.

Figure 3d shows spectra of resonant laser scanning of the bound exciton at both a low power of 7 nW and a high power of 30 nW at 0.5-degree quarter-wave plate angle. For each spectrum, we extract visibility of the interference effect, defined as $\text{Vis} = (I_{\text{tot}} - I_{\text{LO}}) / I_{\text{LO}}$, where I_{tot} is the total reflection intensity and I_{LO} is the local oscillator intensity. The reflection exhibits a strongly nonlinear behavior where at low power we observe a strong interference, which diminishes at higher pump powers. This strong nonlinearity results from the saturation of the bound exciton, which induced a highly nonlinear scattering spectrum with the potential to achieve single emitter mirror³⁶ and low photon number phase shifter³⁷.

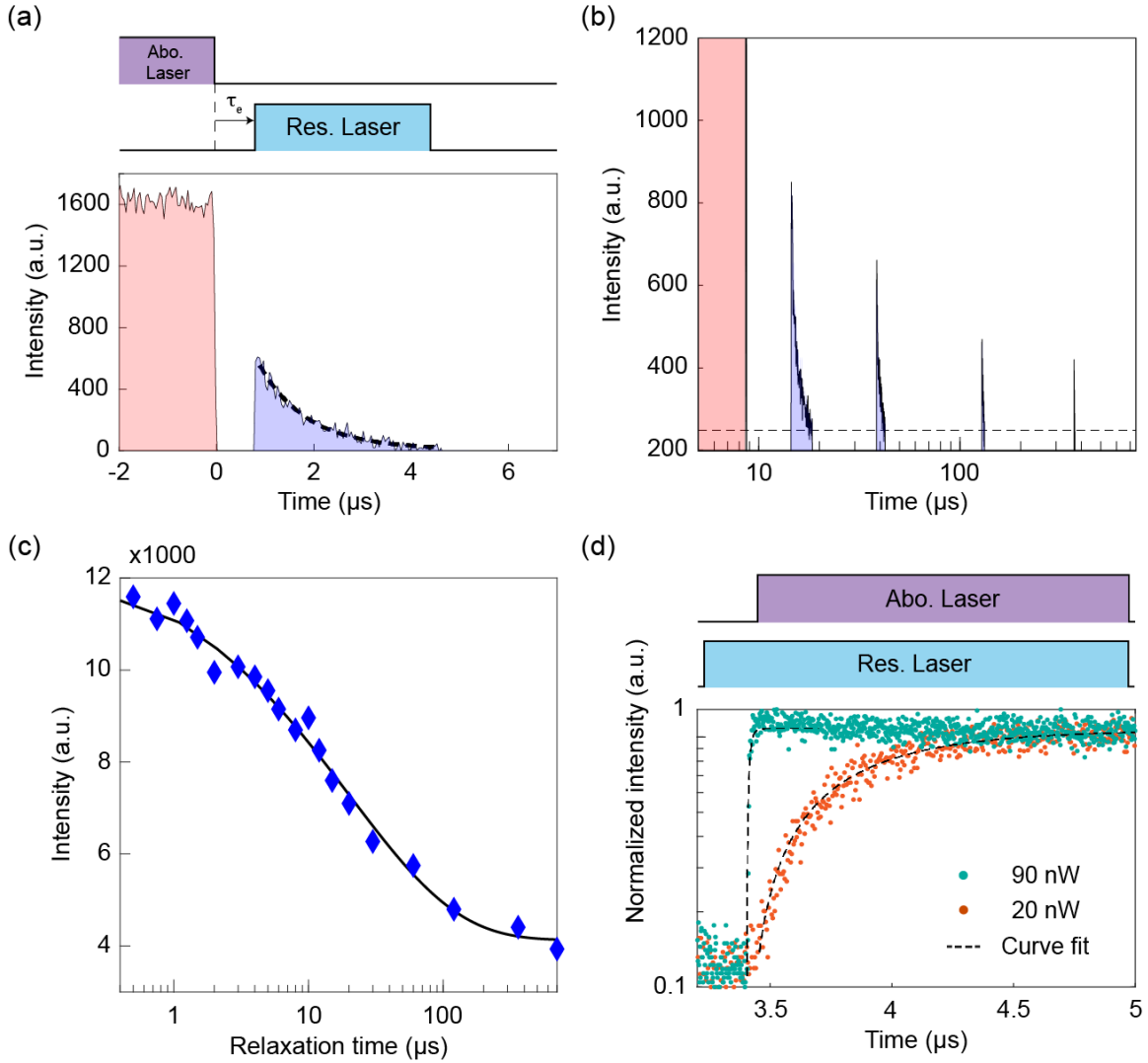


Figure 4. Dynamics of the CI impurity donor-bound exciton resonance fluorescence. (a) Upper panel, Principle of measuring time-resolved resonance fluorescence from the bound exciton. Lower panel, Fluorescence intensity as a function of time. The red-shaded area indicates photoluminescence from above-band excitation, and the blue-shaded area indicates resonance fluorescence from the bound exciton under resonant pumping. There is a 1.2 μs delay between the resonant laser pulse and the above-band excitation. (b) Time-resolved resonance fluorescence of the bound exciton with varied delay time. 4 plots are shown in the figure with a semilogarithmic scale. (c) The integrated intensity of the resonance fluorescence as a function of the delay time. Blue markers show the measured data, and the solid line shows a fit of stretched exponential decay to the measurement. (d) The above-band laser rapidly recovers the resonance fluorescence of the bound exciton. This gating effect is shown at two different above-band laser powers (90 nW, green dots, 20 nW, red dots) with different switching-on rates.

To investigate the dynamics of the impurity state, we perform pulsed excitation measurements. The inset to Figure 4a shows the pulse sequence we use. We first pump the emitter with a 5 μs

above-band laser pulse with an average power of 40 nW in order to charge-stabilize the impurity. We then probe the impurity by exciting it with a 4 μs resonant laser pulse with an adjustable delay time τ_e to generate resonance fluorescence. We generate both pulses by amplitude modulating the continuous wave lasers using an acousto-optic modulator. Additional details are provided in Supplementary Materials Section VI.

Figure 4a shows emission intensity as a function of time for a delay of $\tau_e = 1.2 \mu\text{s}$. We observe direct photoluminescence during the above band pumping period (denoted by the red shaded area), which quickly shuts off when the above-band laser pulse ends. We then observe resonance fluorescence (denoted by blue shaded area) when the resonant laser excites the emitter. Unlike the above-band excitation, resonant excitation quickly decays to zero. By fitting the data into an exponential decay function, we obtain a decay rate of $1.013 \mu\text{s}^{-1}$. This rate increases linearly as a function of the resonant pumping power, as shown by the power dependent measurements in the Supplementary Material Section VI. This linear increase suggests that the decay is due to optically induced discharging via a non-radiative Auger recombination³⁸. In Supplementary Material Section VII, we show that once the emission decays, the impurity remains dark for longer than 20 μs . This long dark time further supports the assertion that the emission quenching is because of discharging, as opposed to a metastable state that would require extremely long excited state lifetimes.

In Figure 4b we plot the same measurement for various delay times τ_e ranging from 0.5 μs to 200 μs . The measurements exhibit a decrease of the resonance fluorescence intensity as delay time increases. Figure 4c plots the integrated emission intensity as a function of the delay time. The data best fit into a stretched exponential decay with a time constant of 21 μs . We attribute this decay to spontaneous discharging of the impurity, which may originate from tunneling to nearby trap states or surface states.

The spontaneous discharging of the impurity is consistent with the measurements shown in Figure 2a, which demonstrate that the impurity requires a small amount of above-band light to stabilize charge. To determine the time scale of this recovery, we utilize the pulse sequence in the inset to Figure 4d. Here we first turn on the resonant laser, and then turn on the above-band laser. The

initial resonant laser will discharge the emitter via Auger recombination, while the non-resonant laser will recharge it, leading to a recovery of signal.

Figure 4d shows the resonance fluorescence intensity using the modified pulse sequence. As anticipated, the emission rapidly recovers at the onset of the above-band laser eventually reaching its maximal value. The figure shows results at above-band powers of 20 nW and 90 nW. We notice that the higher above-band power leads to a signal recovery with a faster time constant. To obtain this time constant, we fit these two curves to a function of $I(t) = I_0(1 - \exp(-t/\tau))$, which reflects the population change of the impurity state. By increasing the above-band power, the recovery time efficiently increases from 200 ns to 9.3 ns. These results demonstrate the potential of short above-band pulses to restore charge to an ionized emitter on nanosecond timescales.

Conclusion

In summary, we present a detailed analysis of coherent resonance-fluorescence emission from a single Cl impurity-bound exciton. By resonantly exciting the impurity we demonstrated bright emission of quantum light with extremely high Debye-Waller factor of 0.94, among the highest values in solid-state defects. We demonstrate the coherence of the fluorescence and probe the impurity state dynamics via resonant excitation and time-resolved fluorescence. Cl impurity donor-bound excitons naturally possess a spin $\frac{1}{2}$ ground state. The resonant excitation methods we present here therefore open up a direct pathway towards optical control and readout of spin. The integration of these emitters with optical cavities could further enable coherent spin-photon interaction¹⁰. Ultimately, this work opens the possibility for direct optical control of impurity bound excitons to achieve efficient quantum light sources and spin-light interfaces.

Methods

Device description

The ZnMgSe/ZnSe/ZnMgSe QW structure was grown using molecular beam epitaxy on a GaAs substrate. The 4.7 nm thick ZnSe QW is enclosed between two 29 nm ZnMgSe barriers, all on top of a 12 nm thick ZnSe buffer layer between the ZnMgSe barriers and the substrate. The Cl donors were incorporated in the ZnSe QW by delta-doping with a low sheet density of 10^{10} cm⁻². To form single isolated Cl-impurities, nanopillars were fabricated in a top-down nanofabrication approach. After sample growth, the nanopillar and the nanolens patterns were defined by using the HSQ negative electron beam resist and a greyscale electron-beam lithography. Then the nanopillar structures were fabricated by dry etching via inductively coupled plasma reactive ion etching with a combination of H₂/Ar/CHF₃ gases, which also forms the spherical nanolens on top of each pillar. Finally, the sidewalls exposed during the dry etching step were polished with a potassium dichromate solution.

Optical measurement setup

Figure 1b shows the schematic of the experimental setup. We mount the sample in a closed-loop cryostat (Attocube, attoDRY 1000). A free-space confocal microscopy is used to both excite the sample and collect the reflected optical signal, with an objective lens which has NA = 0.7. The above-band excitation is achieved by a laser diode (Thorlabs, LP405-SF10). The resonant excitation and the laser scanning are performed by using a tunable diode laser (TOPTICA, DL pro). This tunable laser is sent through polarization-maintained single-mode fiber, and transmits through a linear polarizer, a half-wave plate and a quarter-wave plate. The reflected signal from the sample transmits through another set of quarter-wave plate, half-wave plate and linear polarizer, which is collected by a polarization-maintained single mode fiber and sent for further analysis. The spectra are recorded by a spectrometer (Princeton Instruments), consisting of a liquid nitrogen cooled CCD camera, with a monochromator grating (1714 g/mm). For correlation measurements and the time-resolved measurements, two fiber-based superconducting single photon detectors (PhotonSpot) are used to collect the signals, which is then converted to electric signal and sent to the time-correlated single photon counter (Multiharp 300). We measure the resonance fluorescence second-order correlation in a standard Hanbury Brown and Twiss setup. The emission collected

from the fiber is split by a 50:50 fiber beam splitter and sent to two detectors. The analysis is assisted by the Qucoa (PicoQuant) software.

Cross polarization setup

In the experiments, we excite the emitter with a linear polarized light. The excitation beam from the tunable laser is sent through the fiber and well-collimated by a spherical lens. The linear polarizer and the half-wave plate in the input path are used to align the input beam in a horizontal polarization state $|H\rangle$. Then the reflected signal is collected in an orthogonal state $|V\rangle$, governed by the half-wave plate and the linear polarizer on the output optical path. Two quarter waveplates are used to compensate the chromatic dispersion of the waveplate retardation. The optimized cross-polarization filter achieves the suppression of the input laser light with an extinction ratio exceeding 10^6 .

Acknowledgement

Support is acknowledged from AFOSR grant #FA95502010250 and The Maryland-ARL quantum partnership #W911NF1920181. This work is also funded by the Deutsche Forschungsgemeinschaft (DFG, German Research Foundation) under Germany's Excellence Strategy - Cluster of Excellence Matter and Light for Quantum Computing (ML4Q) EXC 2004/1-390534769.

Competing financial interests

The authors declare no competing financial interests.

Reference

1. Zhukov, E. A. *et al.* Spin coherence of electrons and holes in ZnSe-based quantum wells studied by pump-probe Kerr rotation. *Phys Status Solidi B Basic Res* **251**, 1872–1880 (2014).
2. Gutowski, J., Presser, N. & Kudlek, G. Optical Properties of ZnSe Epilayers and Films. *physica status solidi (a)* **120**, 11–59 (1990).
3. Steiner, T., Thewalt, M. L. W. & Bhargava, R. N. Photoluminescence lifetimes of bound excitons in ZnSe. *Solid State Commun* **56**, 933–936 (1985).
4. Sleiter, D. J. *et al.* Optical pumping of a single electron spin bound to a fluorine donor in a ZnSe nanostructure. *Nano Lett* **13**, 116–120 (2013).
5. Karasahin, A. *et al.* Single quantum emitters with spin ground states based on Cl bound excitons in ZnSe. *Phys Rev A (Coll Park)* **106**, (2022).
6. Pettit, R. M. *et al.* Correlations between Cascaded Photons from Spatially Localized Biexcitons in ZnSe. *Nano Lett* **22**, 9457–9461 (2022).
7. Kutovyi, Y. *et al.* Efficient Single-Photon Sources Based on Chlorine-Doped ZnSe Nanopillars with Growth Controlled Emission Energy. *ACS Nano* **16**, 14582–14589 (2022).
8. Sanaka, K., Pawlis, A., Ladd, T. D., Lischka, K. & Yamamoto, Y. Indistinguishable Photons from Independent Semiconductor Nanostructures. *Phys Rev Lett* **103**, 53601 (2009).
9. Pawlis, A. *et al.* MBE Growth and Optical Properties of Isotopically Purified ZnSe Heterostructures. *ACS Appl Electron Mater* **1**, 44–50 (2019).
10. Jiang, Y., M. Pettit, R., den Driesch, N., Pawlis, A. & Waks, E. Cavity-Enhanced Single-Photon Emission from a Single Impurity-Bound Exciton in ZnSe. *ACS Photonics* **11**, 1103–1108 (2024).
11. Qiao, S. *et al.* Two-dimensional photonic crystal cavities in ZnSe quantum well structures. 1–19 (2024).
12. Astafiev, O. *et al.* Resonance Fluorescence of a Single Artificial Atom. *Science (1979)* **327**, 840–843 (2010).
13. Vamivakas, A. N., Zhao, Y., Lu, C. Y. & Atatüre, M. Spin-resolved quantum-dot resonance fluorescence. *Nat Phys* **5**, 198–202 (2009).
14. Muller, A. *et al.* Resonance fluorescence from a coherently driven semiconductor quantum dot in a cavity. *Phys Rev Lett* **99**, (2007).
15. Chen, D. *et al.* Optical Gating of Resonance Fluorescence from a Single Germanium Vacancy Color Center in Diamond. *Phys Rev Lett* **123**, (2019).
16. Dean, P. J., Fitzpatrick, B. & Bhargava, R. N. *Donor Bound-Exciton Excited States in Zinc Selenide. NUMBER* vol. 23 (1981).
17. Schmitt-Rink, S., Miller, D. A. B. & Chemla, D. S. Theory of the linear and nonlinear optical properties of semiconductor microcrystallites. *Phys. Rev. B* **35**, 8113–8125 (1987).
18. Takagahara, T. Electron-phonon interactions and excitonic dephasing in semiconductor nanocrystals. *Phys. Rev. Lett.* **71**, 3577–3580 (1993).
19. Woggon, U., Gindele, F., Wind, O. & Klingshirn, C. Exchange interaction and phonon confinement in CdSe quantum dots. *Phys. Rev. B* **54**, 1506–1509 (1996).
20. Gindele, F., Hild, K., Langbein, W. & Woggon, U. *Phonon Interaction of Single Excitons and Biexcitons.*

21. Brash, A. J. *et al.* Light Scattering from Solid-State Quantum Emitters: Beyond the Atomic Picture. *Phys Rev Lett* **123**, (2019).
22. Tran, T. T., Bray, K., Ford, M. J., Toth, M. & Aharonovich, I. Quantum emission from hexagonal boron nitride monolayers. *Nat Nanotechnol* **11**, 37–41 (2016).
23. Wang, X. J. *et al.* Quantum Emitters with Narrow Band and High Debye-Waller Factor in Aluminum Nitride Written by Femtosecond Laser. *Nano Lett* **23**, 2743–2749 (2023).
24. Sajid, A., Ford, M. J. & Reimers, J. R. Single-photon emitters in hexagonal boron nitride: a review of progress. *Reports on Progress in Physics* vol. 83 Preprint at <https://doi.org/10.1088/1361-6633/ab6310> (2020).
25. Kuhlmann, A. V. *et al.* Transform-limited single photons from a single quantum dot. *Nat Commun* **6**, (2015).
26. Senellart, P., Solomon, G. & White, A. High-performance semiconductor quantum-dot single-photon sources. *Nature Nanotechnology* vol. 12 1026–1039 Preprint at <https://doi.org/10.1038/nnano.2017.218> (2017).
27. Grijseels, S. C. M. *et al.* Radiative lifetimes and linewidth broadening of single InAs quantum dots in an Al_xGa(1-x)As matrix. *J Lumin* **176**, 95–99 (2016).
28. Berthel, M. *et al.* Photophysics of single nitrogen-vacancy centers in diamond nanocrystals. *Phys Rev B Condens Matter Mater Phys* **91**, (2015).
29. Messin, G., Hermier, J. P., Giacobino, E., Desbiolles, P. & Dahan, M. *Bunching and Antibunching in the Fluorescence of Semiconductor Nanocrystals*. *OPTICS LETTERS* vol. 26 (2001).
30. Efros, A. L. & Rosen, M. *Random Telegraph Signal in the Photoluminescence Intensity of a Single Quantum Dot*. (1997).
31. Santori, C. *et al.* Submicrosecond correlations in photoluminescence from InAs quantum dots. *Phys Rev B Condens Matter Mater Phys* **69**, (2004).
32. Nutz, M. *et al.* Photon Correlation Spectroscopy of Luminescent Quantum Defects in Carbon Nanotubes. *Nano Lett* **19**, 7078–7084 (2019).
33. Fushman, I. *et al.* Controlled phase shifts with a single quantum dot. *Science (1979)* **320**, 769–772 (2008).
34. Wrigge, G., Gerhardt, I., Hwang, J., Zumofen, G. & Sandoghdar, V. Efficient coupling of photons to a single molecule and the observation of its resonance fluorescence. *Nat Phys* **4**, 60–66 (2008).
35. Fano, U. *Effects of Configuration Interaction on Intensities and Phase Shifts**. *REVIEW* vol. 124 (1961).
36. Staunstrup, M. J. R. *et al.* Direct observation of a few-photon phase shift induced by a single quantum emitter in a waveguide. *Nature Communications* **15**, (2024).
37. Chang, D. E., Sørensen, A. S., Demler, E. A. & Lukin, M. D. A single-photon transistor using nanoscale surface plasmons. *Nat Phys* **3**, 807–812 (2007).
38. Nguyen, H. S. *et al.* Photoneutralization and slow capture of carriers in quantum dots probed by resonant excitation spectroscopy. *Phys Rev B Condens Matter Mater Phys* **87**, (2013).